Volume 17
Number 17
7 September 2024
Pages 6129–6422

Energy & Environmental Science

rsc.li/ees

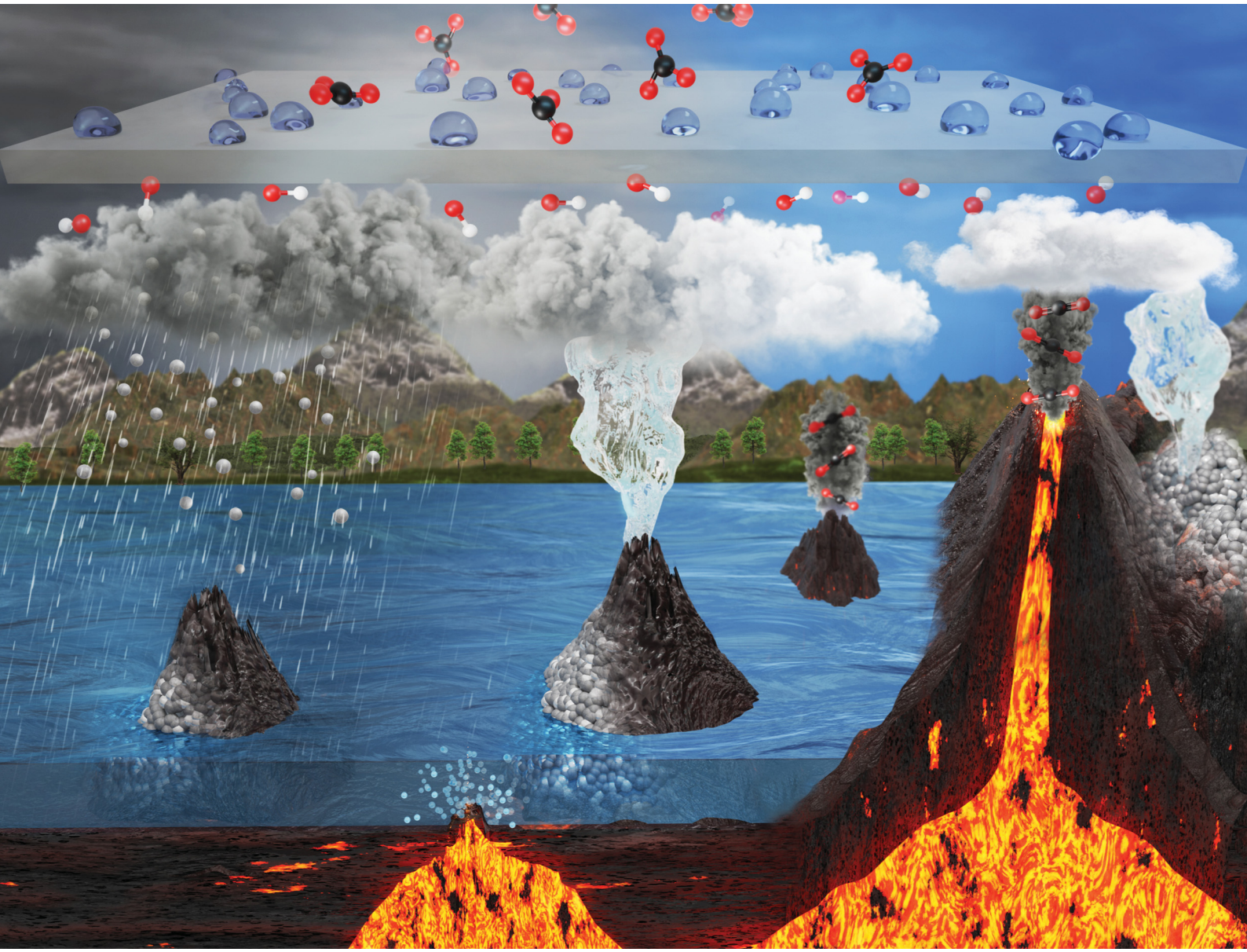

ISSN 1754-5706

ROYAL SOCIETY OF CHEMISTRY

PAPER

Woong Hee Lee, Hyung-Suk Oh *et al.*
Breaking the current limitation of electrochemical CO_2 reduction *via* a silica-hydroxide cycle

Energy & Environmental Science

ROYAL SOCIETY OF CHEMISTRY

PAPER

View Article Online
View Journal | View Issue

Check for updates

Cite this: *Energy Environ. Sci.*, 2024, **17**, 6215

Breaking the current limitation of electrochemical CO_2 reduction *via* a silica-hydroxide cycle†

Chulwan Lim,‡[ab] Sangkuk Kim,‡[ac] Ji Hwan Song,‡[a] Man Ho Han,[a] Young-Jin Ko,[a] Kwan-Young Lee,[b] Jae-Young Choi,[de] Woong Hee Lee*[a] and Hyung-Suk Oh*[ade]

Received 28th January 2024,
Accepted 29th April 2024

DOI: 10.1039/d4ee00448e

rsc.li/ees

Alkaline local pH during a vigorous electrochemical CO_2 reduction reaction (CO_2RR) can improve the activity and selectivity of CO_2RR. However, it also leads to an alkalinity problem in that hydroxide ions obstruct the mass transfer of CO_2 to the active site, thereby limiting the current density. In this study, we introduce a silica-hydroxide cycle, which moderates the local pH by redistributing hydroxide ions, analogous to the carbonate-silicate cycle responsible for the drawdown of atmospheric CO_2 on Earth. In the membrane electrode assembly (MEA) of a CO_2 electrolyzer, SiO_2 undergoes weathering due to the high local pH and consequently consumes OH^-, reducing the pH within the MEA. The dissolved silicate ions move to the membrane and are almost regenerated to SiO_2 with release of OH^-. Geological and spectral observations suggest that the silica-hydroxide cycle reduces the local pH thereby enhancing mass transfer of CO_2, breaking the limitation of current density for CO_2RR. Our work proposes new chemical approaches to increase current density, mainly improved by physical methods, and contributes valuable insight for improving a variety of electrochemical systems.

Open Access Article. Published on 30 2024. Downloaded on 12/10/2024 18:07:24.
This article is licensed under a Creative Commons Attribution-NonCommercial 3.0 Unported Licence.

Broader context

The electrochemical CO_2 reduction reaction (CO_2RR) is viewed as a promising approach to attain carbon neutrality while generating valuable fuels and chemicals. Enhancing the current density in CO_2RR presents a significant challenge for the efficient production of chemicals on a meaningful scale, which is essential for economic viability. Recently, various mechanical approaches have enhanced the performance of CO_2RR through enhancing the mass transfer of CO_2, playing a pivotal role in improving the current density. Nevertheless, in the high current density region, the hydroxide ions created during the reaction form a local alkaline environment, which converts CO_2 to carbonate ions, hindering the mass transfer of CO_2 to the catalyst surface and limiting the current density for CO_2RR. This study delves into the role of SiO_2 in the electrochemical CO_2RR regarding the silica-hydroxide cycle, which moderates the local pH by redistributing hydroxide ions. This mechanism draws a parallel with the silicate-carbonate cycle, which plays a crucial role in the natural sequestration of atmospheric CO_2 on Earth, thus offering a novel avenue for breaking the current density limitation of CO_2RR through controlled pH management.

Introduction

The electrochemical CO_2 reduction reaction (CO_2RR) is viewed as a promising solution for achieving carbon neutrality while producing valuable fuels and chemicals.[1–3] Increasing the current density for CO_2RR poses a significant challenge for the mass production of chemicals while ensuring economic feasibility.[4,5] Recently, various mechanical approaches, including gas-phase CO_2, device design, gas diffusion electrode (GDE), membrane electrode assembly (MEA), pressurized system and nanosized catalyst, have successfully enhanced the performance of CO_2RR *via* enhancing mass transfer of CO_2, playing a pivotal role in improving the current density.[6–17] Under high current density regime coming from a recently developed system, an intriguing phenomenon, called local pH,

[a] *Clean Energy Research Center, Korea Institute of Science and Technology, Hwarang-ro 14-gil 5, Seongbuk-gu, Seoul 02792, Republic of Korea. E-mail: hyung-suk.oh@kist.re.kr, abcabac@kist.re.kr; Tel: +82 (0)2 958 5824*
[b] *Department of Chemical and Biological Engineering, Korea University, 145 Anam-ro, Seongbuk-gu, Seoul, 02841, Republic of Korea*
[c] *Hydrogen and Low-Carbon Energy R&D laboratories, POSCO HOLDINGS, 67 Cheongam-ro, Nam-gu, Pohang-si, Gyeongsangbuk-do, 37673, Republic of Korea*
[d] *School of Advanced Materials Science & Engineering, Sungkyunkwan University (SKKU), Suwon, 16419, Republic of Korea*
[e] *KIST-SKKU Carbon-Neutral Research Center, Sungkyunkwan University (SKKU), Suwon 16419, Republic of Korea*

† Electronic supplementary information (ESI) available. See DOI: https://doi.org/10.1039/d4ee00448e

‡ All authors contributed equally to this work.

Open Access Article. Published on 30 2024. Downloaded on 12/10/2024 18:07:24.
This article is licensed under a Creative Commons Attribution-NonCommercial 3.0 Unported Licence.

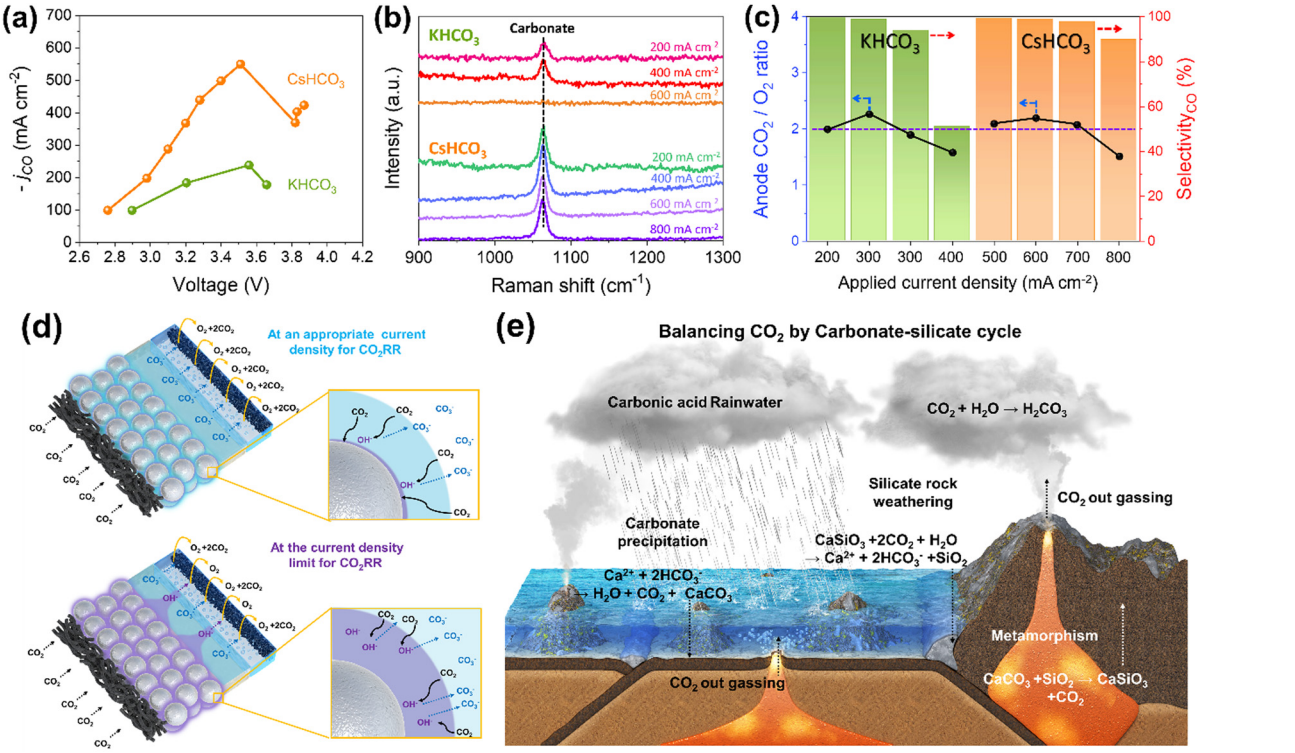

Fig. 1 Alkalinity issue in CO_2RR and carbonate-silicate cycle. (a) CO partial current density *versus* cell voltage in a zero-gap electrolyzer using Ag black with 0.1 M $KHCO_3$ and 0.1 M $CsHCO_3$. (b) *In situ*/*operando* Raman spectroscopy results with 1 M $KHCO_3$ and $CsHCO_3$ electrolytes. (c) CO_2/O_2 ratio at the anode in a zero-gap electrolyzer with 0.1 M $KHCO_3$ and 0.1 $CsHCO_3$. (d) A schematic depiction of the alkalinity problem in a zero-gap CO_2 electrolyzer. (e) A schematic representation of the carbonate-silicate geochemical cycle on Earth.

clearly appeared for CO_2RR. The hydroxide ions generated from the reaction create a local alkaline environment at the electrode, promoting CO_2RR *via* reducing the hydrogen evolution reaction (HER) and modulating binding energies for the intermediates.[18–24] Nevertheless, some studies addressing local pH have indicated an alkalinity problem in that hydroxide ions block the mass transfer of CO_2 to the catalyst by converting carbonate, limiting the current density for CO_2RR.[25,26] The alkalinity problem of CO_2RR can be validated using alkali cation effects. Numerous experimental and theoretical investigations reveal that a larger size of alkali cation exhibits smaller hydration number at the Helmholtz layer and lower pK_a values near the electrode, mitigating the local pH phenomenon.[27–29] The current density of CO_2RR according to alkali cation was assessed in a CO_2 MEA electrolyzer using Ag black sprayed GDE (Fig. 1a and Fig. S1–S3, ESI†). $CsHCO_3$ electrolyte demonstrated a significantly higher maximum current density for CO_2RR than $KHCO_3$ electrolyte. To delve into the pH reaction environment of the cathode in the MEA electrolyzer, *in situ*/*operando* Raman spectroscopy and gas analysis of the anode were carried out (Fig. 1b and c). In the Raman spectra for the $KHCO_3$ electrolyte, the carbonate peak disappeared at current densities exceeding 400 mA cm^{-2}, while the carbonate peak persisted at a current density of 800 mA cm^{-2} using $CsHCO_3$ electrolyte. The *in situ*/*operando* Raman spectroscopy focused on the catalyst surface. Thus, the disappeared carbonate peak indicates that the catalyst surface possesses high alkalinity with almost no carbonate ions resulting from reaction with OH^- and CO_2 gas. These observations indicate that the larger size of Cs cations alleviates the local pH phenomenon at high current densities. The gas ratio of CO_2 and O_2 for the anode side decreased below 2 was observed at 400 mA cm^{-2} for $KHCO_3$ and 800 mA cm^{-2} for $CsHCO_3$. The changes of gas ratio by current density are well explained by the schematic illustration in Fig. 1d. The ratio of CO_2 and O_2 is close 2 in the current density region showing high faradaic efficiency (FE) for CO, indicating the main carbonate ion transfer from cathode to anode.[30,31] The decreased CO_2 at the anode shows transfer of hydroxide ions from the cathode, suggesting a highly alkaline reaction environment at the cathode sufficient to prevent hydroxide ion contact with CO_2. Additionally, as shown in the *in situ*/*operando* Raman results in Fig. 1b, the mass transfer of CO_2 to the catalyst layer is impeded by high local pH, further limiting the current density for CO_2RR. This suggests that, besides physical properties that can be improved by mechanical methods, the chemical reaction environment also plays a significant role in current limitations. Thus, chemical approaches, such as cation effects, are essential for enhancing current density in CO_2RR. The key for a chemical strategy is alleviating local pH by rebalancing CO_2 and hydroxide ion concentration at the cathode.

In nature, Earth's CO_2 is balanced by various carbon cycles including the carbonate-silicate cycle.[32–35] This

 This journal is © The Royal Society of Chemistry 2024

Open Access Article. Published on 30 2024. Downloaded on 12/10/2024 18:07:24.
This article is licensed under a Creative Commons Attribution-NonCommercial 3.0 Unported Licence.

geochemical process redistributes CO_2 in the atmosphere to the oceans and land by rainwater, silicate weathering, carbonate precipitation and sedimentation, resulting in drawdown of atmospheric CO_2 (Fig. 1e) The stored CO_2 in land is redistributed to the atmosphere by volcanism. In this study, we aim to break the current density limitation for CO_2RR using silica oxide *via* a silica-hydroxide cycle, similar to the carbonate-silicate cycle. The unique silica properties allow distribution of the high OH^- concentration at the catalyst surface to the other cathode side, reducing the elevated local pH at the catalyst surface and facilitating mass transfer of CO_2 for CO_2RR.

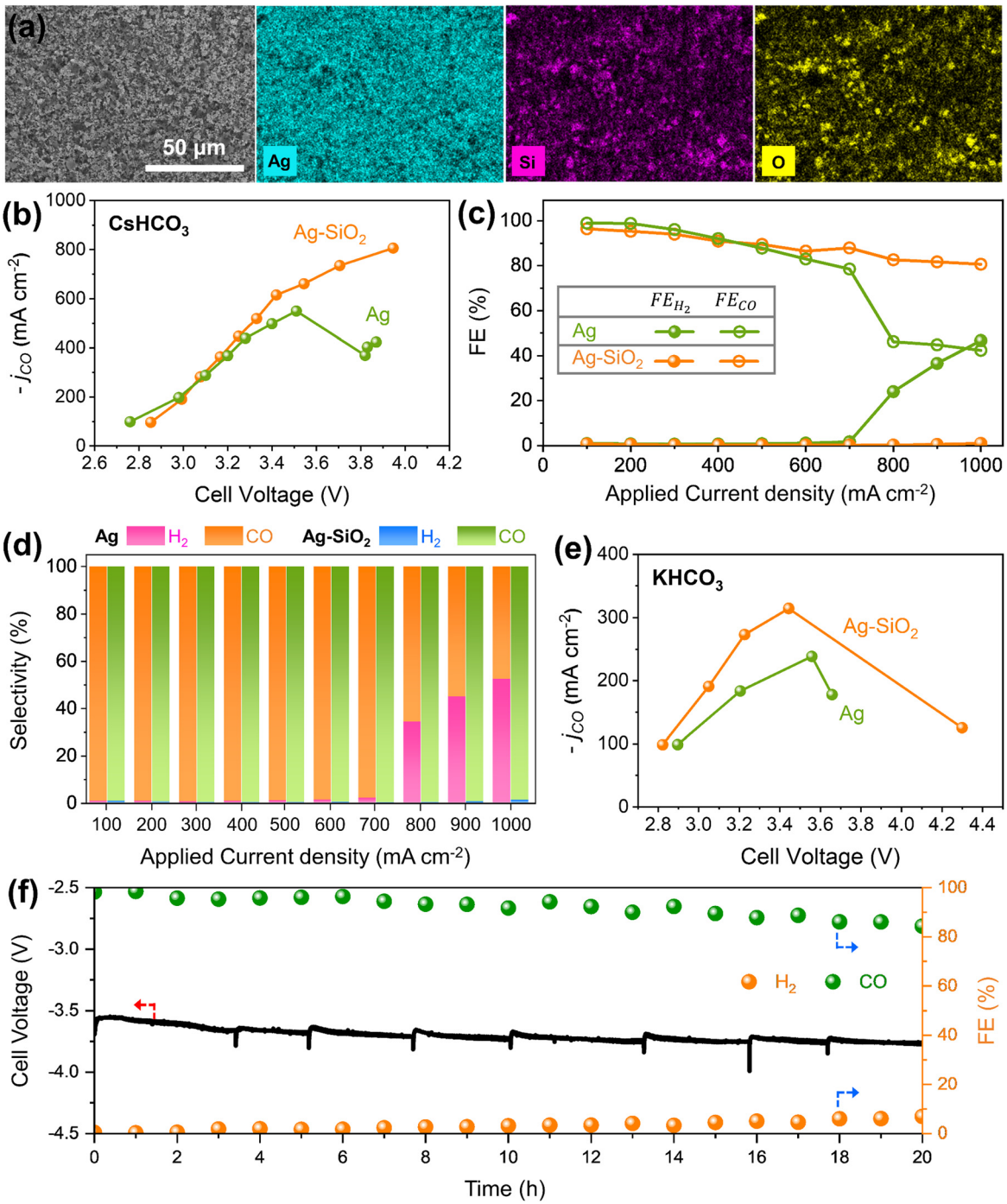

Fig. 2 Impact of SiO_2 in MEA CO_2 electrolyzer, alongside CO_2RR performance comparisons between Ag black and Ag–SiO_2. (a) SEM image and EDS elemental mapping of the Ag–SiO_2 electrode. (b) CO partial current density, (c) H_2 and CO faradaic efficiency, and (d) H_2 and CO selectivity for both Ag black and Ag–SiO_2 using 0.1 M $CsHCO_3$. (e) CO partial current density of Ag black and Ag–SiO_2 with 0.1 M $KHCO_3$. (f) Durability test for Ag–SiO_2 in the zero-gap electrolyzer using 0.1 M $CsHCO_3$ at 700 mA cm^{-2} for 12 h.

Open Access Article. Published on 30 2024. Downloaded on 12/10/2024 18:07:24.
This article is licensed under a Creative Commons Attribution-NonCommercial 3.0 Unported Licence.

Results and discussion

Effects of SiO_2 on current density for CO_2RR

An Ag–SiO_2 electrode was fabricated on a GDE by spraying ink of a mixture of SiO_2 nanopowder and commercial Ag black (Fig. S4–S6, ESI†). Fig. 2a illustrates SEM and SEM-EDX mapping images of the Ag–SiO_2 electrode, indicating that Ag black and SiO_2 nanoparticles are well dispersed on the GDE substrate. The effects of SiO_2 for CO_2RR performance were studied by using an anion exchange membrane (AEM) zero-gap electrolyzer with 0.1 M $CsHCO_3$ anolyte and humidified CO_2 gas (Fig. 2b, d and Fig. S7, ESI†).[36,37] At an applied current density below 600 mA cm^{-2}, both the Ag and Ag–SiO_2 electrodes show similar CO_2RR performance, with a high FE_{CO} exceeding 90%. However, above an applied current density of 700 mA cm^{-2}, the FE_{H2} of the Ag electrode drastically increased with rising current density, resulting in a maximum current density for CO of 549 mA cm^{-2}. On the other hand, the FE_{CO} for the Ag–SiO_2 electrode remained at over 80% and the selectivity for CO (H_2 and CO, SE_{CO}) was nearly 100% at an applied current density until 1 A cm^{-2} while suppressing the HER. The difference of FE_{CO} and SE_{CO} at a high current density region would come from production of formate (Fig. S8, ESI†). The maximum current density of the Ag–SiO_2 electrode for CO reached a value of 806 mA cm^{-2}, implying that additional SiO_2 to the Ag black electrode contributed to breaking the current density limitation for CO_2RR. Exploring the effects of varying SiO_2 ratios indicates the necessity for an optimal amount of SiO_2 (Fig. S9, ESI†). To confirm the physical effects, an Ag–TiO_2 electrode was fabricated using similar size of TiO_2 instead of SiO_2 (Fig. S10, ESI†). Ag–TiO_2 exhibits a similar limiting current density to Ag for CO_2RR. The results of Ag–TiO_2 and the comparable ECSA value for both the Ag and Ag–SiO_2 electrodes show that the impact of SiO_2 does not originate from physical properties (Fig. S11 and S12, ESI†). A similar phenomenon of breaking the maximum current density limit for CO_2RR was observed using 0.1 M $KHCO_3$ anolyte at lower current densities (Fig. 2e and Fig. S13, ESI†). To validate the SiO_2 effects for high current density, chronopotentiometry tests were conducted at a current density of 700 mA cm^{-2} where the effect of SiO_2 is seen (Fig. 2f and Fig. S14, ESI†). FE_{CO} of the Ag electrode was close to 80% and rapidly decreased after 3 h. In contrast, the Ag–SiO_2 electrode demonstrated stable cell voltage and consistent FE_{CO} above 90% for 12 h, suggesting that the effects of SiO_2 are not an instant phenomenon and could serve as a sustained strategy.

The origin of SiO_2 effects in breaking current density limitation

To elucidate the origins of SiO_2 effects that overcome the current density limitation of CO_2RR, the cathode reaction

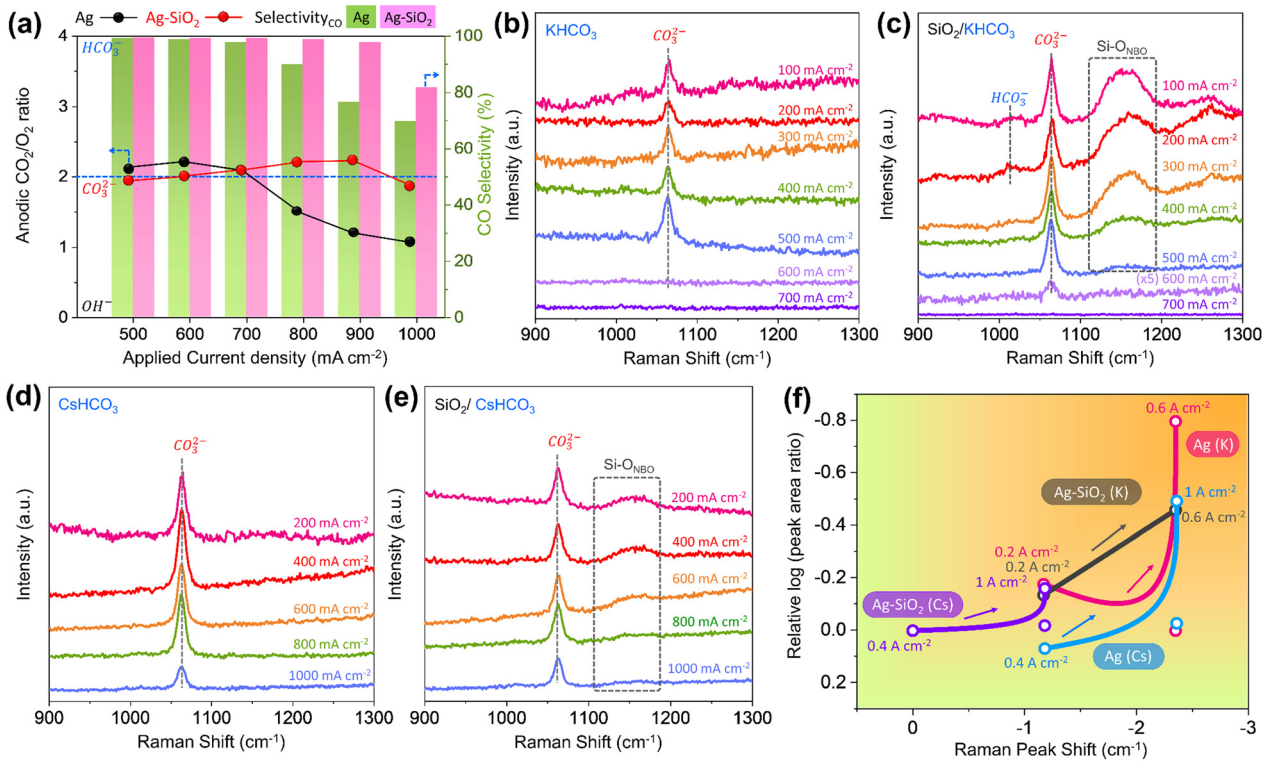

Fig. 3 The analyses of the role of SiO_2 in modulating the cathode reaction environment. (a) CO_2/O_2 ratio at the anode in a zero-gap electrolyzer using Ag–SiO_2 with 0.1 M $CsHCO_3$. (b) *In situ*/*operando* Raman spectroscopy results for the Ag electrode in 1 M $KHCO_3$ electrolyte. (c) *In situ*/*operando* Raman spectroscopy results for the Ag–SiO_2 electrode in 1 M $KHCO_3$ electrolyte. (d) *In situ*/*operando* Raman spectroscopy results for the Ag electrode in 1 M $CsHCO_3$ electrolyte. (e) *In situ*/*operando* Raman spectroscopy results for the Ag–SiO_2 electrode in 1 M $CsHCO_3$ electrolyte. (f) Summary of *in situ*/*operando* Raman spectroscopy results using carbonate Raman peak shifts and carbonate peak intensity ratios for both Ag and Ag–SiO_2 electrodes in $KHCO_3$ and $CsHCO_3$ electrolytes. Reference points for peak shift and intensity: $KHCO_3$, 100 mA cm^{-2}; $CsHCO_3$, 200 mA cm^{-2}.

 This journal is © The Royal Society of Chemistry 2024

Open Access Article. Published on 30 2024. Downloaded on 12/10/2024 18:07:24.
This article is licensed under a Creative Commons Attribution-NonCommercial 3.0 Unported Licence.

environment in the MEA electrolyzer was investigated using gas analysis of the anode and *in situ*/*operando* Raman spectroscopy using a GDE. For the Ag–SiO_2 electrode, the gas composition ratio of CO_2 to O_2 remains near 2 within a current density range of 500–1000 mA cm^{-2}. However, for the Ag electrode, this ratio drops to almost 1 when the current density exceeds 800 mA cm^{-2} (Fig. 3a). This suggests that SiO_2 mitigates the local pH effects stemming from high current densities.

To more directly observe the reaction environment of the cathode, *in situ*/*operando* Raman spectroscopy was carried out using a customized GDE Raman cell (Fig. S15, ESI†).[38] To estimate the pH of the cathode according to current density, we constructed two calibration curves for ranges of 9–13 and 13–14 (Fig. S16–S20, ESI†). Even at a low current density of 100 mA cm^{-2}, the bicarbonate peak for all *in situ*/*operando* Raman spectra nearly disappears, signifying pronounced local pH effects in the GDE.[23] In a $KHCO_3$ electrolyte, the carbonate peak disappears for the Ag electrode at a current density of 600 mA cm^{-2} (Fig. 3b). Conversely, for the Ag–SiO_2 electrode, a minor carbonate peak persists at the same current density, indicating that SiO_2 mitigates local pH effects, reminiscent of cation effects (Fig. 3c). The Ag–SiO_2 electrode also exhibited a similar trend in $CsHCO_3$ electrolyte. The carbonate peak for the Ag electrode is lower than that for the Ag–SiO_2 electrode at a current density of 1 A cm^{-2} (Fig. 3d and e).

For the Ag–SiO_2 electrode, peaks corresponding to Si–O_{NBO} (where NBO is non-bridging oxygen) were observed at a current density between 100 and 400 mA cm^{-2}, hinting at the onset of SiO_2 degradation in alkaline conditions (Fig. S21, ESI†).[39,40] For intuitive representation of local pH under various conditions,

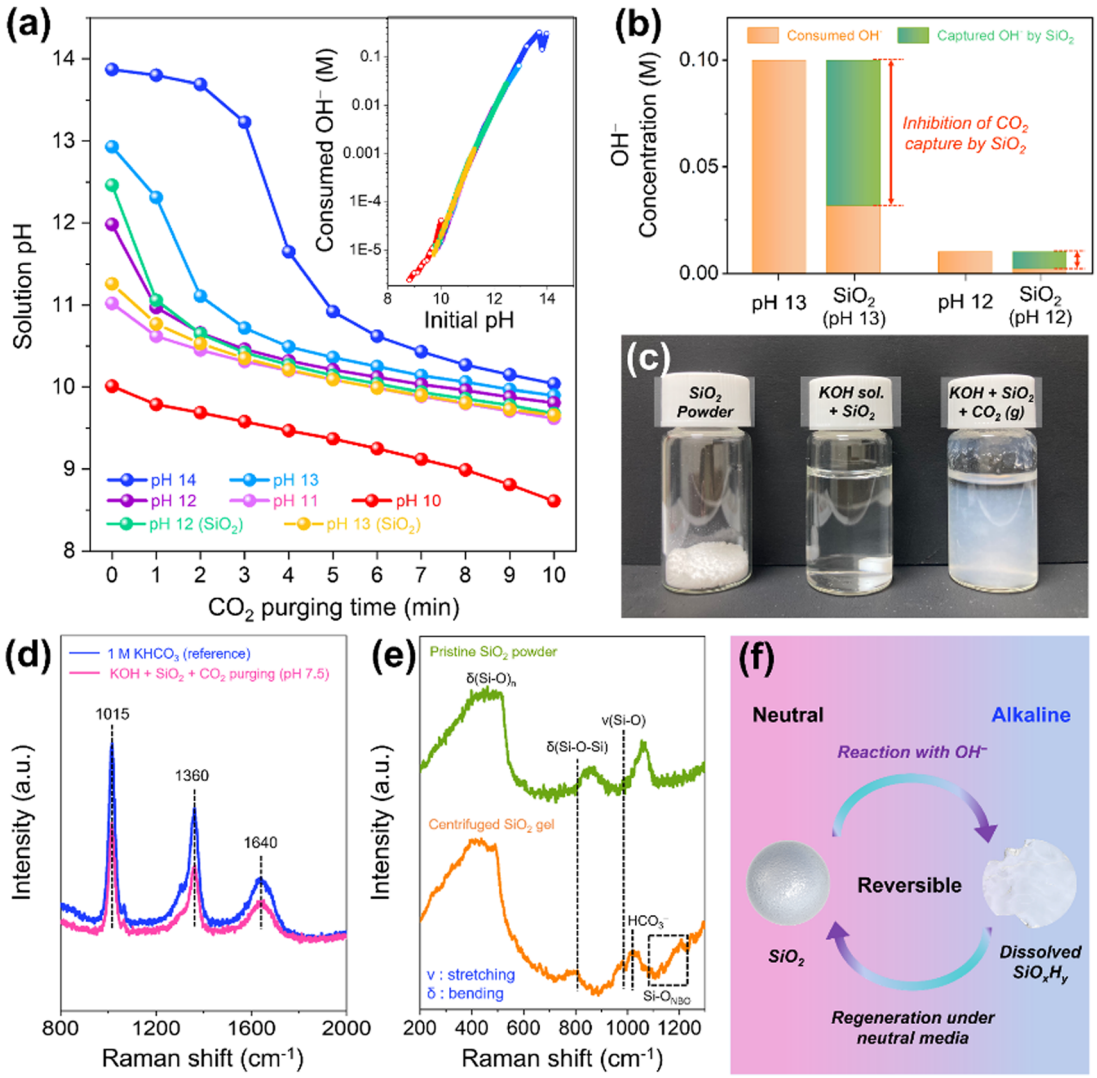

Fig. 4 Analysis of SiO_2 in CO_2RR media. (a) Change in solution pH for various initial pH solutions under CO_2 purge, plotted against CO_2 purging time (Inset: Quantity of OH^- consumed based on current pH). (b) Variation in OH^- concentration during CO_2 purging, attributed to OH^- capture due to the presence of SiO_2. (c) Images of pristine SiO_2 powder, SiO_2-dissolved KOH solution, and an opaque gel obtained within the SiO_2-dissolved KOH solution after CO_2 purging. (d) Raman spectra comparing 1 M $KHCO_3$ solution (reference), and the CO_2-purged, SiO_2-dissolved KOH solution (containing the opaque gel). (e) Raman spectra comparing pristine SiO_2 powder and centrifuged SiO_2 gel obtained from the opaque gel within the CO_2-purged solution. (f) A schematic illustrating the reversible behavior of SiO_2 species during the reaction.

Open Access Article. Published on 30 2024. Downloaded on 12/10/2024 18:07:24.
This article is licensed under a Creative Commons Attribution-NonCommercial 3.0 Unported Licence.

we summarize the *in situ*/*operando* Raman results based on two parameters: the log-transformed relative peak area ratio of the carbonate peak and its shift (Fig. 3f). The carbonate peak shift is expected to be related to the Stark effect or cation concentration.[41–43] However, since there is no carbonate intermediate in the CO_2RR mechanism on the Ag surface, we assumed that this peak shift was caused by cation concentration. The calibration results unequivocally show that carbonate peak area, which is related to carbonate concentration, is correlated to pH and peak shift corresponds to cation concentration (Fig. S22 and S23 and Note S2, ESI†). Based on calibration data, the estimated local pH results from *in situ*/*operando* Raman spectra are shown in Fig. S24 and Table S1 (ESI†). While the alkalinity of the Ag electrode increased with current density, the Ag–SiO_2 electrode in comparison retained its pH, underscoring the role of SiO_2 in the suppression of local pH effects.

Behavior of SiO_2 in CO_2RR system

In an effort to understand the effects of SiO_2, it is necessary to observe the behavior of SiO_2 in a medium that simulates the

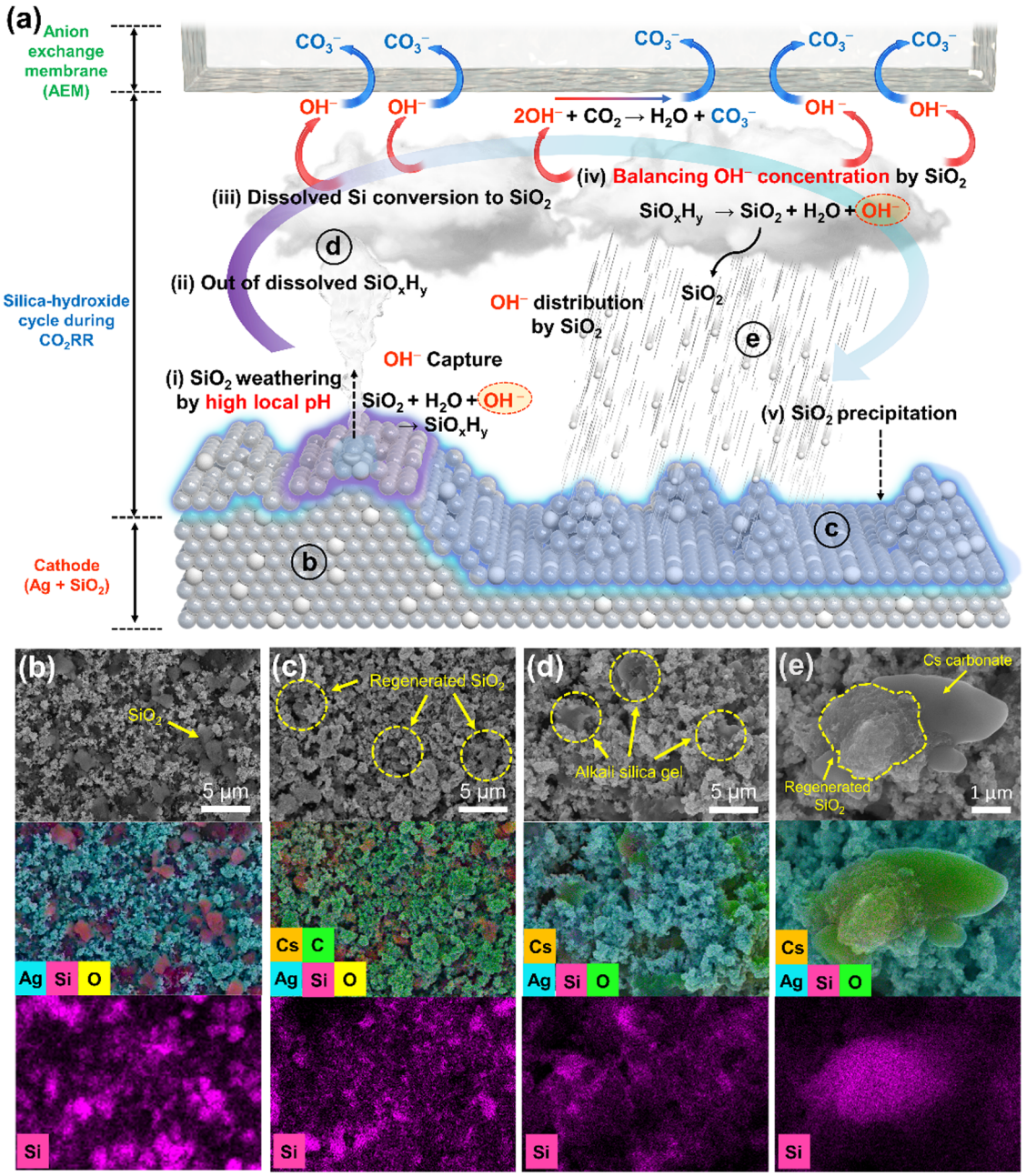

Fig. 5 Geological and spectral observations of silica-hydroxide cycle in MEA CO_2 electrolyzer. (a) A schematic representation of the carbonate-silicate geochemical cycle occurring during electrochemical CO_2 reduction reaction on Ag–SiO_2. SEM images and EDS elemental mapping of the Ag–SiO_2 electrode before (b) and after (c)–(e) reaction (c: 900 mA cm^{-2} for 20 min; (d) and (e): 1 A cm^{-2} for 20 min) in MEA CO_2 electrolyzer.

 This journal is © The Royal Society of Chemistry 2024

Open Access Article. Published on 30 2024. Downloaded on 12/10/2024 18:07:24.
This article is licensed under a Creative Commons Attribution-NonCommercial 3.0 Unported Licence.

reaction environment for a CO_2 MEA electrolyzer. To verify the neutralization of local pH by CO_2, we purged the CO_2 gas into solutions of various pH and measured the pH every minute (Fig. 4a). As the duration of the CO_2 purge increased, the solution's pH decreased, owing to the reaction of OH^- ions with CO_2, resulting in carbonate ions. The amount of consumed OH^- with CO_2 is proportional to pH of solution, highlighting the alkalinity problem that blocks the transfer of CO_2 to active sites due to the high local pH. When the SiO_2 nanopowder was mixed with alkaline solution of pH 12 and 13, SiO_2 dissolved, leading to a decrease in the solution's pH. Regardless of the presence of SiO_2, the rate of OH^- consumption by CO_2 was invariably proportional to the pH of the solution, implying that CO_2 gas capture by OH^- is suppressed by SiO_2 (Fig. 4b). Interestingly, suspensions were detected in SiO_2-dissolved solution following an extended CO_2 purge (Fig. 4c). The analysis of collected solution and precipitate (by centrifugation) after 2 h of CO_2 purge (the pH of solution reached 7.5) demonstrates separation of SiO_2 and $KHCO_3$ solution,[44] suggesting almost reversible behavior of SiO_2 (Fig. 4d, e and Fig. S21, S25, ESI†). When the SiO_2 nanopowder was mixed with solutions of 0.1 M $KHCO_3$ (pH 8.65) and 1 M $KHCO_3$ (pH 8.69), the pH remained almost unchanged at 8.70 (Fig. S26, ESI†). The presumed reaction involving SiO_2 is depicted in Fig. 4f. In alkaline media, SiO_2 dissolved and converted to silicate ions by reaction of OH^-. These silicate ions then precipitate as SiO_2 under neutral conditions with release of OH^- due to low solubility.[44–46] We hypothesize that this cycle involving SiO_2 and hydroxide also takes place in the CO_2 MEA electrolyzer.

The silica-hydroxide cycle in MEA CO_2 electrolyzer

The mechanism of breaking the current limitation by SiO_2 in a CO_2 electrolyzer is hypothesized as being due to the reversible cycle of SiO_2 between alkaline and neutral media, carrying OH^- ions (Fig. 5a). We postulate that this silica-hydroxide cycle decreases the local pH of the electrode surface by increasing hydroxide distribution, thereby enhancing mass transfer of CO_2 for CO_2RR. This process of silica-hydroxide cycle is similar to the silicate-carbonate cycle that maintains the CO_2 level in the atmosphere. When a vigorous CO_2RR occurs in the MEA CO_2 electrolyzer, the pH of catalyst surface is presumed to be that of an alkaline medium in the range of pH 11–14 by *in situ*/*operando* Raman spectroscopy. Concurrently, the pH of the AEM is expected to be neutral owing to abundant transported carbonate ions, indicating a suitable environment for the reversible silica-hydroxide cycle.

To demonstrate the silica-hydroxide cycle in the MEA CO_2 electrolyzer, silica weathering, evidence of the silica-hydroxide cycle, was monitored using geological and spectral observations with SEM. The pristine Ag–SiO_2 electrode clearly delineates the boundary between SiO_2 and Ag nanoparticles (Fig. 5b and Fig. S27, ESI†). After CO_2RR, this boundary becomes less distinct in SEM images (Fig. 5c and Fig. S28, ESI†), and this blurring intensifies as the current density increases (Fig. S29–S33, ESI†). Nevertheless, SiO_2 is well dispersed in the electrode, similar to before the reaction. Notably, no discernible difference in Ag nanoparticles dependent on SiO_2 is observed, suggesting that SiO_2 has no effect on the chemical state and structure of Ag (Fig. S34–S39, ESI†). These outcomes corroborate the hypothesis of silica weathering under high current densities. To further substantiate the presence of dissolved silicate ions and the regeneration of SiO_2, EDS mapping was employed to discern the state of SiO_2. When the dissolved silicate ions dried with alkali cations, hydrous alkali silica gel is formed.[47] This hydrous alkali silica gel is observed in certain regions of the electrode, signifying the presence of dissolved silicate ions (Fig. 5d and Fig. S40, ESI†). The accumulation of regenerated SiO_2 on the Ag electrode, the final step of the silica-hydroxide cycle, is clearly shown in Fig. 5e. SiO_2 appears on the Cs carbonate precipitate that is generated during or post-CO_2RR, implying regenerated SiO_2.

Under high cathodic currents, SiO_2 weathering is triggered by high local pH, leading to a decrease in pH by consuming OH^- at the catalyst surface. The dissolved silicate ions, not reacted with CO_2, move to the AEM side.[48,49] The dissolved silicate ions are converted to SiO_2 with counterbalancing release of OH^- under neutral conditions at the AEM and the converted SiO_2 is redistributed on the electrode. However, the silica-hydroxide cycle is not completely reversible in the MEA electrolyzer owing to the AEM, which is highly permeable to anions and cations. SEM-EDS mapping cross-section images after reaction show that the majority of SiO_2 remains in the cathode, but a small amount of SiO_2 has been moved to the AEM and anode (Fig. S41, ESI†). To eliminate the regeneration step at the AEM, 1 M KOH was used for MEA test instead of 0.1 M $CsHCO_3$ at a current density of 700 mA cm^{-2}. ICP-OES analysis shows that 67.6% of SiO_2 is preserved on the cathode with the silica-hydroxide cycle but, without the regeneration step, 5.8% of Si remained on the cathode. These results show that the regeneration step, which is critical for reversibility of the silica-hydroxide cycle, functions in a real MEA electrolyzer. This silica-hydroxide cycle reduces the concentration of OH^- that captures CO_2, thereby enhancing mass transfer of CO_2 to catalyst active sites and breaking the limitation of current density.

Conclusions

Our study introduces a novel strategy to overcome the limitation of the current density for CO_2RR by a chemical cycle approach, without the need for physical modification. Hydroxide ions generated from CO_2RR elevate the local pH. While this can enhance selectivity, it also hinders the transfer of CO_2 by forming carbonate ions, thus imposing a current density limitation for CO_2RR. Therefore, controlling the local pH is crucial for achieving a high current density. On Earth, atmospheric CO_2 levels are reduced *via* carbon cycles, such as the silicate-carbonate cycle. This geological carbon cycle redistributes CO_2 from the atmosphere to rocks through silicate weathering. Similarly, the silica-hydroxide cycle derived using

Open Access Article. Published on 30 2024. Downloaded on 12/10/2024 18:07:24.
This article is licensed under a Creative Commons Attribution-NonCommercial 3.0 Unported Licence.

SiO_2 causes a reduction in the local pH of the catalyst surface in the MEA CO_2 electrolyzer. SiO_2 weathering is triggered by high local pH, and silicate ions transport the hydroxide ions near the AEM without CO_2 capture at the catalyst surface and reconvert to SiO_2. This cycle of SiO_2 enhances the mass transfer of CO_2, breaking the current density limitation for CO_2RR. Considering commercialization, the future goals of the silica-hydroxide cycle should be focused on enhancing the reversibility in real MEA electrolyzers. This chemical cycle strategy also observed on Earth holds a wide-ranging applicability across various systems, offering fresh insights for augmenting their efficiency and breaking their limitations.

Experimental procedures

Materials and chemicals

Silver nanopowder (Alfa Aesar, APS 20–40 nm, 99.9%), silicon dioxide nanopowder (Sigma-Aldrich, 10–20 nm, 99.5% trace metal basis), titanium(IV) oxide nanopowder (Sigma-Aldrich, 21 nm primary particle size (TEM), ≥99.5% trace metals), Nafion 5 wt% ionomer solution (Sigma-Aldrich), isopropanol (DAEJUNG, 99.5%), and iridium(IV) oxide (Alfa Aesar, premion, 99.99%; Ir 84.5% min) were used as received, without further purification. Carbon paper (Fuel Cell Store, Sigracet 39BB) and platinized titanium screen (Fuel Cell Store) were employed as substrates for cathodic and anodic electrodes, respectively. These substrates were cut to the desired size using a home-made punch. $KHCO_3$, which was used as the electrolyte, was procured from Sigma Aldrich (ACS reagent, >99.7%). The AEM used was sourced from Dioxide Materials (Sustainion X37-50 grade RT).

Preparation of Ag-based electrode for cathode

The Ag black, Ag–TiO_2 and Ag–SiO_2 electrodes were fabricated by spraying catalyst ink onto a gas diffusion layer (GDL) at 70 °C. For the Ag–SiO_2 catalyst ink, 90 mg of commercial silver nanopowder, 15 mg of silicon dioxide nanopowder, 120 mg of Nafion ionomer solution, and 3.5 mL of isopropanol were ultrasonically mixed. Ag–TiO_2 catalyst ink was fabricated with same method as for Ag–SiO_2 catalyst ink except for adding TiO_2 instead of SiO_2. The catalyst ink for Ag black was prepared using the same method as for Ag–SiO_2, but without the silicon dioxide nanopowder.

Preparation of Ir-based electrode for anode

The electrode for OER, employed as the anode, was fabricated by spraying catalyst ink onto a platinized titanium screen using a 70 °C hot plate. The catalyst ink was prepared by mixing 120 mg of commercial iridium oxide (Alfa Aesar) with 120 mg of 5 wt% Nafion ionomer solution and 4 mL of isopropanol. The electrode had an area of 10 cm^2, and the iridium oxide loading was set at 2 mg cm^{-2}.

Single-cell electrochemical CO_2 reduction reaction test

MEAs were fabricated using the catalyst-coated electrode method for electrochemical reactions, and the geometric electrode area was set at 10 cm^2. The fabricated electrodes, along with commercial IrO_2-sprayed platinized titanium screen electrodes (Alfa Aesar, with a target loading of 2.0 mg cm^{-2}), were employed as cathodes and anodes in all single-cell tests, respectively. The AEM (Dioxide Materials, X37-50 Grade RT) underwent pretreatment in a 1 M KOH solution for 48 h and was rinsed multiple times with deionized water before use. Following this, a 0.1 M $KHCO_3$ solution, acting as the electrolyte, was introduced to the anode side *via* a pump. Concurrently, 200 sccm of humidified CO_2 gas at 80 °C, heated using a mantle, was introduced to the cathode side. The electrochemical tests were conducted using a VSP potentiostat (BioLogic, VMP3B-20) equipped with a booster up to 20 A. The CO_2RR was conducted over 18 min for each applied current density.

A gas chromatograph (GC, Agilent 7890A) was employed for product gas analysis at the GC outlet. A water trap was interposed between the GC and the cathode outlet. Argon gas (99.999%) served as the carrier gas. The GC was fitted with a flame ionization detector (FID) to detect hydrocarbons like CO, CH_4, and C_2H_4, and a thermal conductivity detector (TCD) for hydrogen (H_2) gas detection. A methanizer was utilized to enhance CO detection before routing to the FID. Measurements of the product gases commenced 9 min after initiation of CO_2RR for each current density setting. The FEs of H_2 and CO were computed using the following equation:

$$\mathrm{FE}_{\mathrm{product}}\,(\%) = \frac{i_{\mathrm{product}}}{i_{\mathrm{total}}} \times 100 = \frac{V_{\mathrm{product}} \times Q \times \frac{2Fp}{RT}}{i_{\mathrm{total}}} \times 100$$

where Q = flow rate of the product: F = faradaic constant (96 485 C mol^{-1}): p = pressure: T = room temperature (298 K): R = ideal gas constant (8.314 J mol^{-1} K^{-1}).

The partial current densities of the products were determined from the volume of a specific product, as indicated by the GC peak.

Physical characterization

The size distribution and microstructure of the Ag black and Ag–SiO_2 electrodes were examined using high-resolution transmission electron microscopy (HR-TEM, Titan at 300 kV, FEI Co., USA). HR-TEM images, high-angle annular dark-field scanning transmission electron microscopy (HAADF-STEM) images, and energy-dispersive spectroscopy (EDS) mapping were performed with a Talos F200X system (FEI). Raman spectroscopy was employed to characterize various electrodes, powdered samples, and the prepared solutions, and was conducted at room temperature with a 532-nm laser (Renishaw). XPS (X-ray photoelectron spectroscopy, Nexsa, ThermoFisher Scientific) was conducted with a base pressure of 2×10^{-8} mbar and a monochromated Al Kα (1486.6 eV) X-ray source. All XPS spectra were calibrated using the C 1s peak (284.8 eV) as a reference.

In situ/*operando* Raman spectroscopy

In situ/*operando* SERS (surface-enhanced Raman spectroscopy) was conducted using a standard three-electrode system, a custom-made *in situ* Raman cell (details provided in Fig. S14,

 This journal is © The Royal Society of Chemistry 2024

Open Access Article. Published on 30 2024. Downloaded on 12/10/2024 18:07:24.
This article is licensed under a Creative Commons Attribution-NonCommercial 3.0 Unported Licence.

ESI†), and a laser with a 532-nm wavelength. The working electrode was fashioned by spraying catalyst ink (containing Ag and Ag–SiO_2 powders) onto a GDL (Sigracet 39BB, SGL Carbon) substrate, which amplified the Raman spectrum signal. A Pt wire and Ag/AgCl (3 M NaCl) served as the counter and reference electrodes, respectively. The electrolyte was either 1 M $KHCO_3$ or 1 M $CsHCO_3$, and gaseous CO_2 was purged onto the working electrode at a flow rate controlled with a ball flowmeter. The electrochemical experiments were controlled using a potentiostat (CompactStat, Ivium Technologies, Eindhoven, Netherlands). The thin electrolyte layer enveloping the electrode facilitated Raman spectroscopic observation of the working electrode's surface.

Author contributions

C. L., S. K. and J. H. S. designed/conducted the experiments, analyzed the data and wrote the manuscript. M. H. H. performed Raman analysis of Ag black and Ag–SiO_2. Y.-J. K. contributed to the electrochemical cell tests. K. Y. L. and J. Y. C. provided an idea for the electrochemical analysis. H.-S. O. and W. H. L. supervised the research and wrote the manuscript. All authors reviewed the manuscript.

Conflicts of interest

There are no conflicts to declare.

Acknowledgements

This work was supported by institutional program grants from the Korea Institute of Science and Technology (KIST) and Research Project for 'Carbon Upcycling Project for Platform Chemicals' of the National Research Foundation (NRF) funded by the Ministry of Science and ICT (grant number: 2022M3J3A1050053) and 'Carbon to X Project' (project no. 2020M3H7A1098229) through the National Research Foundation (NRF) funded by the Ministry of Science and ICT, Republic of Korea. This research was also supported by the National Research Council of Science & Technology (NST) grant by the Korean government (MSIT) (no. CAP21011-100) and National Research Foundation of Korea (NRF) grant funded by the Korean government (MSIT) (NRF-2021R1A6A3A01086623, RS-2023-00256847).

References

1 W. H. Lee, K. Kim, J. H. Koh, D. K. Lee, D. H. Won, H.-S. Oh, U. Lee and B. K. Min, *Nano Energy*, 2023, **110**, 108373.
2 I. E. L. Stephens, K. Chan, A. Bagger, S. W. Boettcher, J. Bonin, E. Boutin, A. K. Buckley, R. Buonsanti, E. R. Cave, X. Chang, S. W. Chee, A. H. M. da Silva, P. de Luna, O. Einsle, B. Endrődi, M. Escudero-Escribano, J. V. Ferreira de Araujo, M. C. Figueiredo, C. Hahn, K. U. Hansen, S. Haussener, S. Hunegnaw, Z. Huo, Y. J. Hwang, C. Janáky, B. S. Jayathilake, F. Jiao, Z. P. Jovanov, P. Karimi, M. T. M. Koper, K. P. Kuhl, W. H. Lee, Z. Liang, X. Liu, S. Ma, M. Ma, H.-S. Oh, M. Robert, B. R. Cuenya, J. Rossmeisl, C. Roy, M. P. Ryan, E. H. Sargent, P. Sebastián-Pascual, B. Seger, L. Steier, P. Strasser, A. S. Varela, R. E. Vos, X. Wang, B. Xu, H. Yadegari and Y. Zhou, *J. Phys.: Energy*, 2022, **4**, 042003.
3 S. Jin, Z. Hao, K. Zhang, Z. Yan and J. Chen, *Angew. Chem.*, 2021, **133**, 20795–20816.
4 J. Na, B. Seo, J. Kim, C. W. Lee, H. Lee, Y. J. Hwang, B. K. Min, D. K. Lee, H.-S. Oh and U. Lee, *Nat. Commun.*, 2019, **10**, 5193.
5 M. Jouny, W. Luc and F. Jiao, *Ind. Eng. Chem. Res.*, 2018, **57**, 2165–2177.
6 L. Ge, H. Rabiee, M. Li, S. Subramanian, Y. Zheng, J. H. Lee, T. Burdyny and H. Wang, *Chem*, 2022, **8**, 663–692.
7 M. B. Ross, P. De Luna, Y. Li, C.-T. Dinh, D. Kim, P. Yang and E. H. Sargent, *Nat. Catal.*, 2019, **2**, 648–658.
8 R. I. Masel, Z. Liu, H. Yang, J. J. Kaczur, D. Carrillo, S. Ren, D. Salvatore and C. P. Berlinguette, *Nat. Nanotechnol.*, 2021, **16**, 118–128.
9 B. Endrodi, E. Kecsenovity, A. Samu, F. Darvas, R. Jones, V. Török, A. Danyi and C. Janáky, *ACS Energy Lett.*, 2019, **4**, 1770–1777.
10 D. Higgins, C. Hahn, C. Xiang, T. F. Jaramillo and A. Z. Weber, *ACS Energy Lett.*, 2019, **4**, 317–324.
11 C. M. Gabardo, A. Seifitokaldani, J. P. Edwards, C.-T. Dinh, T. Burdyny, M. G. Kibria, C. P. O'Brien, E. H. Sargent and D. Sinton, *Energy Environ. Sci.*, 2018, **11**, 2531–2539.
12 D. Wakerley, S. Lamaison, J. Wicks, A. Clemens, J. Feaster, D. Corral, S. A. Jaffer, A. Sarkar, M. Fontecave, E. B. Duoss, S. Baker, E. H. Sargent, T. F. Jaramillo and C. Hahn, *Nat. Energy*, 2022, **7**, 130–143.
13 J. Li, G. Chen, Y. Zhu, Z. Liang, A. Pei, C.-L. Wu, H. Wang, H. R. Lee, K. Liu, S. Chu and Y. Cui, *Nat. Catal.*, 2018, **1**, 592–600.
14 D. Kim, Y. Chae, U. Lee, W. Kim and D. H. Won, *Curr. Opin. Electrochem.*, 2023, **39**, 101295.
15 Y. C. Tan, W. K. Quek, B. Kim, S. Sugiarto, J. Oh and D. Kai, *ACS Energy Lett.*, 2022, **7**, 2012–2023.
16 K. Yang, R. Kas, W. A. Smith and T. Burdyny, *ACS Energy Lett.*, 2021, **6**, 33–40.
17 W. Choi, Y. Choi, E. Choi, H. Yun, W. Jung, W. H. Lee, H.-S. Oh, D. H. Won, J. Na and Y. J. Hwang, *J. Mater. Chem. A*, 2022, **10**, 10363–10372.
18 Y. Y. Birdja, E. Pérez-Gallent, M. C. Figueiredo, A. J. Göttle, F. Calle-Vallejo and M. T. M. Koper, *Nat. Energy*, 2019, **4**, 732–745.
19 B. Endrődi, A. Samu, E. Kecsenovity, T. Halmágyi, D. Sebők and C. Janáky, *Nat. Energy*, 2021, **6**, 439–448.
20 M. C. O. Monteiro, A. Mirabal, L. Jacobse, K. Doblhoff-Dier, S. C. Barton and M. T. M. Koper, *JACS Au*, 2021, **1**, 1915–1924.
21 M. Luo, Z. Wang, Y. C. Li, J. Li, F. Li, Y. Lum, D.-H. Nam, B. Chen, J. Wicks, A. Xu, T. Zhuang, W. R. Leow, X. Wang, C.-T. Dinh, Y. Wang, Y. Wang, D. Sinton and E. H. Sargent, *Nat. Commun.*, 2019, **10**, 5814.

Open Access Article. Published on 30 2024. Downloaded on 12/10/2024 18:07:24.
This article is licensed under a Creative Commons Attribution-NonCommercial 3.0 Unported Licence.

22 N. Govindarajan, A. Xu and K. Chan, *Science*, 2022, **375**, 379–380.
23 Z. Zhang, L. Melo, R. P. Jansonius, F. Habibzadeh, E. R. Grant and C. P. Berlinguette, *ACS Energy Lett.*, 2020, **5**, 3101–3107.
24 Y. C. Tan, K. B. Lee, H. Song and J. Oh, *Joule*, 2020, **4**, 1104–1120.
25 C. Chen, Y. Li and P. Yang, *Joule*, 2021, **5**, 737–742.
26 E. W. Lees, B. A. W. Mowbray, F. G. L. Parlane and C. P. Berlinguette, *Nat. Rev. Mater.*, 2022, **7**, 55–64.
27 F. Zhang and A. C. Co, *Angew. Chem., Int. Ed.*, 2020, **59**, 1674–1681.
28 M. R. Singh, Y. Kwon, Y. Lum, J. W. Ager, III and A. T. Bell, *J. Am. Chem. Soc.*, 2016, **138**, 13006–13012.
29 S. Ringe, E. L. Clark, J. Resasco, A. Walton, B. Seger, A. T. Bell and K. Chan, *Energy Environ. Sci.*, 2019, **12**, 3001–3014.
30 G. O. Larrazábal, P. Strøm-Hansen, J. P. Heli, K. Zeiter, K. T. Therkildsen, I. Chorkendorff and B. Seger, *ACS Appl. Mater. Interfaces*, 2019, **11**, 41281–41288.
31 M. Ma, E. L. Clark, K. T. Therkildsen, S. Dalsgaard, I. Chorkendorff and B. Seger, *Energy Environ. Sci.*, 2020, **13**, 977–985.
32 R. G. Hilton and A. J. West, *Nat. Rev. Earth Environ.*, 2020, **1**, 284–299.
33 D. E. Penman, J. K. Caves Rugenstein, D. E. Ibarra and M. J. Winnick, *Earth-Sci. Rev.*, 2020, **209**, 103298.
34 A. Bufe, N. Hovius, R. Emberson, J. K. C. Rugenstein, A. Galy, H. J. Hassenruck-Gudipati and J.-M. Chang, *Nat. Geosci.*, 2021, **14**, 211–216.
35 C. S. Cockell, T. Bush, C. Bryce, S. Direito, M. Fox-Powell, J. P. Harrison, H. Lammer, H. Landenmark, J. Martin-Torres and N. Nicholson, *Astrobiology*, 2016, **16**, 89–117.
36 M. H. Han, D. Kim, S. Kim, S.-H. Yu, D. H. Won, B. K. Min, K. H. Chae, W. H. Lee and H.-S. Oh, *Adv. Energy Mater.*, 2022, **12**, 2201843.
37 W. H. Lee, Y.-J. Ko, Y. Choi, S. Y. Lee, C. H. Choi, Y. J. Hwang, B. K. Min, P. Strasser and H.-S. Oh, *Nano Energy*, 2020, **76**, 105030.
38 Y.-J. Ko, J.-Y. Kim, W. H. Lee, M. G. Kim, T.-Y. Seong, J. Park, Y. Jeong, B. K. Min, W.-S. Lee, D. K. Lee and H.-S. Oh, *Nat. Commun.*, 2022, **13**, 2205.
39 J.-L. You, G.-C. Jiang, H.-Y. Hou, H. Chen, Y.-Q. Wu and K.-D. Xu, *J. Raman Spectrosc.*, 2005, **36**, 237–249.
40 A. Osipov, L. Osipova and R. Zainullina, *Int. J. Spectrosc.*, 2015, **2015**, 572840.
41 W. W. Rudolph, D. Fischer and G. Irmer, *Appl. Spectrosc.*, 2006, **60**, 130–144.
42 Y. Ma, W. Yan, Q. Sun and X. Liu, *Geosci. Front.*, 2021, **12**, 1018–1030.
43 M. Moradzaman and G. Mul, *ChemElectroChem*, 2021, **8**, 1478–1485.
44 J. H. M. Visser, *Cem. Concr. Res.*, 2018, **105**, 18–30.
45 A. N. Palmer and M. V. Palmer, *Speleogenesis and Evolution of Karst Aquifers*, 2003, vol. **1**, pp. 1–8.
46 B. Lagerblad and J. Trägårdh, *Conceptual model for concrete long time degradation in a deep nuclear waste repository*, Swedish Nuclear Fuel and Waste Management Co., Sweden, 1994.
47 R. B. Figueira, R. Sousa, L. Coelho, M. Azenha, J. M. de Almeida, P. A. S. Jorge and C. J. R. Silva, *Constr. Build. Mater.*, 2019, **222**, 903–931.
48 S.-Y. Pan, E. Chang and P.-C. Chiang, *Aerosol Air Qual. Res.*, 2012, **12**, 770–791.
49 M. Santoro, F. Gorelli, J. Haines, O. Cambon, C. Levelut and G. Garbarino, *Proc. Natl. Acad. Sci. U. S. A.*, 2011, **108**, 7689–7692.

 This journal is © The Royal Society of Chemistry 2024